Quantifying symmetric exchange in ultrathin ferromagnetic films with chirality

Tobias Böttcher,[1,2] T. S. Suraj,[3,*] Xiaoye Chen,[4,*] Banibrato Sinha,[1] Hui Ru Tan,[4] Hang Khume Tan,[4] Robert Laskowski,[5] Burkard Hillebrands,[1] Mikhail Kostylev,[6] Khoong Hong Khoo,[5] Anjan Soumyanarayanan,[4,3,†] and Philipp Pirro[1,†]

[1]*Fachbereich Physik and Landesforschungszentrum OPTIMAS, Technische Universität Kaiserslautern, 67663 Kaiserslautern, Germany*

[2]*MAINZ Graduate School of Excellence, 55128 Mainz, Germany*

[3]*Department of Physics, National University of Singapore, Singapore 117551, Singapore*

[4]*Institute of Materials Research & Engineering, Agency for Science, Technology & Research, Singapore 138634, Singapore*

[5]*Institute of High Performance Computing, Agency for Science, Technology & Research, Singapore 138632, Singapore*

[6]*Department of Physics M013, The University of Western Australia, Crawley 6009, WA, Australia*

(Received 4 August 2022; revised 22 December 2022; accepted 20 January 2023; published 8 March 2023)

The symmetric (Heisenberg) exchange interaction is fundamental to magnetism and assumes critical importance in designing magnetic materials for novel emergent phenomena and device applications. However, quantifying exchange is extremely challenging for ultrathin magnetic films, as techniques and approximations reliably used for bulk materials are largely inapplicable in the two-dimensional limit. Here we present and contrast the measurement of exchange stiffness A by several methods on a series of five Co/Pt-based ultrathin (1–2 nm) films. We compare results from (a) spin-wave spectroscopy by Brillouin light scattering, (b) three analytical models describing the temperature dependence of magnetization obtained by magnetometry, (c) microscopic domain periodicity measurements and simulations, and (d) *ab initio* density functional theory calculations. While different methods present some qualitatively consistent trends across samples, we note, for any given sample, considerable differences (up to 5×) in the absolute values of A across the techniques, consistent with discrepancies of A reported in literature for nominally similar samples. We analyze possible sources of the discrepancies across various methods, notably including their relationship to the spin-wave dispersion, and the wave-vector ranges probed. We compare the strengths and limitations of the techniques, and outline directions for their future use in characterizing exchange interactions in ultrathin films.

DOI: 10.1103/PhysRevB.107.094405

I. INTRODUCTION

In recent years, there has been rapid growth of interest on understanding the behavior of magnetic films with thicknesses approaching the two-dimensional (2D) or atomic limit. On one hand, multilayered films interfacing such ultrathin ferromagnets (FMs) with heavy metals give rise to new, emergent phenomena, including chirality, topology, and spin-charge conversion [1–3]. On the other hand, spintronic devices developed from such ultrathin multilayers have attractive properties for memory and computing applications [4–7].

Emergent phenomena in ultrathin magnetic films are governed by magnetic interactions arising at the atomic scale [1]. First, the exchange stiffness A, which, within the micromagnetic description, represents the direct (Heisenberg) exchange interaction between neighboring spins, and characterizes the overall strength of FM order [8,9]. Second, the effective anisotropy K_{eff}, which determines the energetically favoured FM orientation—in-plane (IP), or out-of-plane (OP)—and includes crystalline, shape, and interfacial contributions [9,10]. Third, the Dzyaloshinskii-Moriya interaction (DMI) D, which arises from interfacial effects in asymmetric multilayers, and endows ultrathin magnets with chirality [11–13]. The interplay of these interactions may result in a ground state comprising noncollinear nanoscale spin textures, including chiral domain walls and skyrmions [14–19]. At larger length-scales ($\gtrsim$100 nm), this may additionally include contributions from magnetostatic, or dipolar effects [5]. In order to design material systems with desired ground states or functional devices with specified characteristics, it is imperative to quantify these key interactions within ultrathin magnetic films.

The anisotropy K_{eff} of ultrathin films can be measured straightforwardly via magnetometry or microwave spectroscopy [10], while the DMI (D) is typically determined via the asymmetry in spin-wave or domain propagation (some of which implicitly require A) [13]. In contrast, despite being the most fundamental of the interactions, the exchange stiffness, A is extremely challenging to quantify in the ultrathin limit for several reasons. First, conventional methods used to determine A for thick films—e.g., via resonance modes [20,21]—are either inapplicable in the 2D limit or cannot be implemented due to signal-to-noise constraints. Second, while magnetometry-based approaches utilizing the Bloch law are commonly used

*These authors contributed equally to this work.
†Corresponding authors: anjan@imre.a-star.edu.sg, ppirro@physik.uni-kl.de

for quantifying A [22], the validity of the underlying three-dimensional (3D) model is questionable for the ultrathin limit, and consensus on mitigating this issue is lacking [23,24]. Finally, spin-wave spectroscopy—widely regarded as the most reliable method [25]—has seen limited use for quantifying A in ultrathin chiral films, likely due to constraints imposed by anisotropy, or by dipolar interactions for multiple stack repetitions [26]. Together, these challenges have resulted in large discrepancies in published values of A for nominally similar ultrathin FMs [9,22,24,27]. This lack of consensus is especially concerning given the critical role of A in stabilizing conventional (FM) and novel (chiral) states [3,5], governing magnetoresistive memory and spin-wave device characteristics [7,28], and determining other critical design parameters for functional materials. Therefore, it is imperative to quantitatively benchmark the determination of A values for ultrathin magnetic films across key characterization techniques.

In this paper, we present and contrast the exchange stiffness A determined for five Co/Pt-based ultrathin films using various methods. First, Brillouin light scattering (BLS) spectroscopy was used to measure the spin-wave dispersion, whose analysis, with supporting measurements, enabled the extraction of A. Next, magnetometry measurements were used to obtain the temperature dependence of magnetization, which were analyzed using different variants of the Bloch model adapted to ultrathin films, which provided an independent estimate of A. Furthermore, microscopic domain periodicity measurements, as well as *ab initio* density functional theory (DFT) calculations were also performed for selected cases and compared with experimental results. While qualitative trends across samples are apparent, for a given sample, we note large differences in the magnitude of A obtained by the various methods. We discuss possible origins of these discrepancies, as well as the strengths and limitations of the individual techniques. Finally, we outline principled experimental approaches for the future use of these techniques in characterizing ultrathin films.

The remainder of this paper is structured as follows. In Sec. II, we briefly describe the physical basis for the various characterization methods used to determine A as relevant to ultrathin films; in Sec. III, we present the results of these methods applied to a set of five Co/Pt-based ultrathin film samples. Following this, we compare in Sec. IV the results from different methods, and discuss sources of discrepancies, and conclude in Sec. V by outlining directions for future quantitative efforts.

II. METHODS FOR EXCHANGE DETERMINATION

A. Spin-wave dispersion from BLS spectroscopy

BLS spectroscopy utilises the inelastic scattering of photons with magnons and is an established method for the experimental investigation of spin wave dispersion in magnetic thin films for wave vectors k up to $\sim$25 rad/μm [25]. In recent years, BLS spectroscopy has been used extensively to measure the interfacial DMI in chiral multilayers [22,23,26,29]. In contrast, the corresponding symmetric exchange interaction has received scant attention for ultrathin films likely due to the concomitant presence of interlayer interactions, which are notably absent in this paper.

The dispersion of spin waves propagating perpendicular to the static magnetization within the plane of a homogeneous, ultrathin film, saturated IP, can be treated within the description by Kalinikos and Slavin [30]. For chiral magnetic films, interfacial DMI leads to an asymmetry in the spin-wave dispersion, that is linear in k [29]. Meanwhile, the symmetric part of the dispersion allows for the extraction of the Heisenberg exchange stiffness [31], and is described by [26]

$$\begin{aligned} f(k)_{\mathrm{sym}} &= (f_{\mathrm{SW}}(k) + f_{\mathrm{SW}}(-k))/2 \\ &= \frac{\gamma\mu_0}{2\pi}[(H_{\mathrm{ext}} + \lambda_{\mathrm{ex}}k^2 + M_{\mathrm{S}}\mathrm{g}(kt)) \\ &\quad \cdot (H_{\mathrm{ext}} - H_{\mathrm{U}} + \lambda_{\mathrm{ex}}k^2 + M_{\mathrm{S}}(1 - \mathrm{g}(kt)))]^{1/2}, \quad (1) \end{aligned}$$

where γ is the gyromagnetic ratio of the material, t is the film thickness, and M_{S} is the saturation magnetization. The uniaxial anisotropy field $\mu_0 H_{\mathrm{U}} = 2K_{\mathrm{U}}/M_{\mathrm{S}}$ is related to the uniaxial anisotropy constant K_{U}. This should not be confused with the effective anisotropy constant $K_{\mathrm{eff}} = K_{\mathrm{U}} - 1/2\mu_0 M_{\mathrm{S}}^2$ and the effective anisotropy field $H_{\mathrm{K}} = H_{\mathrm{U}} - M_{\mathrm{S}}$.

The influence of the symmetric exchange is contained in the spin-wave stiffness $\lambda_{\mathrm{ex}} = 2A/(\mu_0 M_{\mathrm{S}})$ with the Heisenberg exchange stiffness A. In addition, the term $\mathrm{g}(x) = 1 - [1 - \exp(-|x|)]/|x|$ accounts for the dipolar interaction between magnetic moments. In order to correctly determine A, one needs to duly consider the additional contributions, e.g., from dipolar interactions, anisotropy etc. In particular, the method requires accurate knowledge of M_{S} and γ, which need to be measured using additional methods. Finally, for ultrathin magnetic bilayers (e.g., Fe/Co), the dispersion relation needs to be described using an effective approach for A (see Appendix).

B. Temperature dependence of saturation magnetization

The temperature dependence of M_{S} of a material, accessible to magnetometry techniques, can be utilized to extract A [8,9,32]. Given its extensive usage in this regard, especially for chiral magnetic films [22,23], we examine this technique in detail, including an overview of possible analytical approaches. For temperatures T well below the Curie temperature T_{c}, the variation of $M_{\mathrm{S}}(T)$ results primarily from the excitation of thermal spin waves. This can be understood by analyzing the spin-wave dispersion across frequencies up to the THz range, with the thermal population of the states described by Bose-Einstein statistics. Within this framework, the dispersion model used and the associated spin-wave density of states (DOS) $\rho(\omega)$ play important roles, where ω is the spin-wave frequency. For the case of a three-dimensional (3D) bulk sample with parabolic dispersion, i.e., $\omega(k) = \gamma\mu_0\lambda_{\mathrm{ex}} \cdot k^2 = 2\gamma(A/M_{\mathrm{S}}) \cdot k^2$ (i.e., $\rho(\omega) \propto \sqrt{\omega}$), neglecting dipolar interactions, anisotropies, and DMI, we obtain the well-known Bloch $T^{3/2}$ law [24,33]

$$M_{\mathrm{S}}(T)_{T^{3/2}} = M_{\mathrm{S}}(0) - 2\mu_B \cdot \eta \cdot \left(\frac{k_{\mathrm{B}} T M_{\mathrm{S}}(0)}{2\gamma A\hbar}\right)^{3/2}, \quad (2)$$

where $M_{\mathrm{S}}(0) \equiv M_{\mathrm{S}}(T = 0)$ and η is a dimensionless prefactor.

The Bloch law is particularly suitable for describing the $M_S(T)$ character of bulk samples at low temperatures [34], where $\eta \simeq 0.0587$ [9,24]. In this case, using the Bloch law to determine A, via a fit to Eq. (2), requires the quantitative determination of $M_S(0)$. While Bloch's $T^{3/2}$ law has been used to quantify exchange for nanometer-thick films [22], some have questioned its validity in the ultrathin regime, as the reduced dimensionality strongly influences the spin-wave DOS [23,32,35]. Consequently, several papers employed a modified Bloch law [23,36,37], for instance, by renormalizing the factor η to account for the altered magnon density in the ultrathin limit [23]. In the following section, we estimate A for our $t = 1(2)$ nm films using values determined for NiFe films, i.e., $\eta \approx 0.3(0.17)$ [23]. However, we caution that such an approach is still limited by the $T^{3/2}$ dependence of $M_S(T)$ derived for 3D systems. Overall, a generalization of the 3D Bloch law approach to ultrathin ferromagnets is inherently challenging.

A more intuitive approach has been proposed for ultrathin films, which explicitly incorporates their 2D character within the $M_S(T)$ expression [24]. As a first approximation, it appears sufficient to consider only the fundamental spin-wave mode, which has a uniform profile over the film thickness. The simplest dispersion for such a 2D model is given by $\omega(k) = \omega_0 + 2\gamma A/M_S(0)k^2$ [24]. For this dispersion, $\rho(\omega)$ is a constant in 2D, proportional to $M_S(0)/A$. Notably, the inclusion of a frequency gap ω_0, due to dipolar interactions, anisotropies and external fields, is critical to model a finite M_S for $T > 0$ [38]. This results in the expression [24]

$$M_S(T)_{2D} = M_S(0)\left[1 - \frac{\mu_B k_B T}{4\pi\gamma A t\hbar}\ln\left(\frac{k_B T}{\hbar\omega_0}\right)\right]. \quad (3)$$

In this case (cf. Bloch law), the determination of A requires knowledge of the film thickness (t), but is independent of $M_S(0)$.

However, the 2D model needs considerable improvement if thickness modes are significantly populated [35]. Even for nanometer thick films, the thermal population of perpendicular standing spin-wave (PSSW) modes can be considerable at temperatures typically usually used in magnetometry measurements. An estimate of their contribution can be obtained by considering the Bose-Einstein distribution $N(\omega)$ with

$$N(\omega_n) = \frac{1}{\exp\left(\frac{\hbar\omega_n}{k_B T}\right) - 1} \quad (4)$$

with the PSSW frequencies

$$\omega_n = 2\gamma(A/M_S)\cdot\left(\frac{n\cdot\pi}{t}\right)^2. \quad (5)$$

For $t = 2$ nm, $M_S = 1200$ kA/m, and $A = 6$ pJ/m, we estimate the first PSSW mode with a wave vector component $k_\perp^{(1)} = \pi/t$ perpendicular to the film plane to be $\omega_1 \approx 2\pi\times 1.3$ THz. Likewise, the second PSSW mode ($k_\perp^{(2)} = 2\pi/t$) $\omega_2 \approx 2\pi\times 5.5$ THz. Hence, assuming the fundamental mode, $\omega_0 \approx 2\pi\times 20$ GHz, the relative occupation of the PSSW modes at RT is $N(\omega_1)/N(\omega_0) = 1.3\%$ and $N(\omega_2)/N(\omega_0) = 0.2\%$. Higher PSSW modes would have considerably lower occupation. Thus, while it appears necessary to account for PSSW modes to adequately describe the $M_S(T)$ reduction, the first two modes seem to be sufficient. Using instead a pure 2D model that neglects PSSW modes would underestimate the magnon density and, thereby, the $M_S(T)$ reduction, ultimately resulting in an underestimate of A.

The contribution of the thermal population of PSSW modes to the $M_S(T)$ reduction can be described by models accounting individually for the influence of each mode [24,32]. Considering the first three modes as per above, the $M_S(T)$ reduction is given by [24,32]

$$M_S(T)_{PSSW} = M_S(0)\left[1 - \sum_{n=0}^{2}\frac{\mu_B k_B T}{4\pi\gamma A t\hbar}\ln\left(\frac{\exp(\hbar\omega_n/k_B T)}{\exp(\hbar\omega_n/k_B T) - 1}\right)\right]. \quad (6)$$

We note that the spin-wave dispersion deviates from the assumed parabolic shape towards the BZ boundary [compare Fig. 1(a)]. Therefore, all approaches presented above are valid only at temperatures low enough that thermal excitations of high-k magnon states can be neglected. This fact can be illustrated for the 2D case by examining the spin-wave DOS, which governs $M_S(T)$ [see Fig. 1(b)]. In particular, Fig. 1(a) compares two spin-wave dispersion models for a 2D square lattice, calculated using $\omega_0 = 2\pi\times 10$ GHz, $M_S = 1200$ kA/m, $A = 10$ pJ/m, and lattice constant $a = 3$ Å, consistent with typical ultrathin metallic ferromagnets [9]. Figure 1(b) evidences the implications of using the parabolic approximation to evaluate the spin-wave DOS for the Bloch law. While the DOS for the parabolic model is constant, that for the full dispersion model increases with frequency. Consequently, with increasing temperature, the full model populates more states of higher frequency, and due to its increasingly larger DOS, $M_S(T)$ decreases faster than for the parabolic model. Therefore, any $M_S(T)$ model assuming parabolic dispersion [e.g., Eqs. (2), (3), and (6)] underestimates the spin-wave DOS and, thereby the $M_S(T)$ reduction, leading to a larger predicted M_S for a given A and T. As a result, these models consistently underestimate A, which stabilizes ferromagnetic order against thermal fluctuations.

Meanwhile, interfacial DMI has negligible influence on the DOS [Fig. 1(b), blue curve, $D = 2$ mJ/m^2]. Hence, we expect that for $M_S(T)$-based estimation of A of ultrathin magnetic films from, both IP and OP measurements can be treated equally to good approximation. Finally, in the context of $M_S(T)$ analysis, it is noteworthy that both the Bloch $T^{3/2}$ law, and the other models discussed here are formulated for T-independent exchange stiffness A.

C. Domain periodicity

In chiral multilayers, the microscopic domain characteristics are determined by the competition between D and A. For multilayers exhibiting a labyrinthine domain state at remanence, it is established that the measured domain periodicity can be compared with micromagnetic simulations to determine the ratio of A and D. An independent determination of

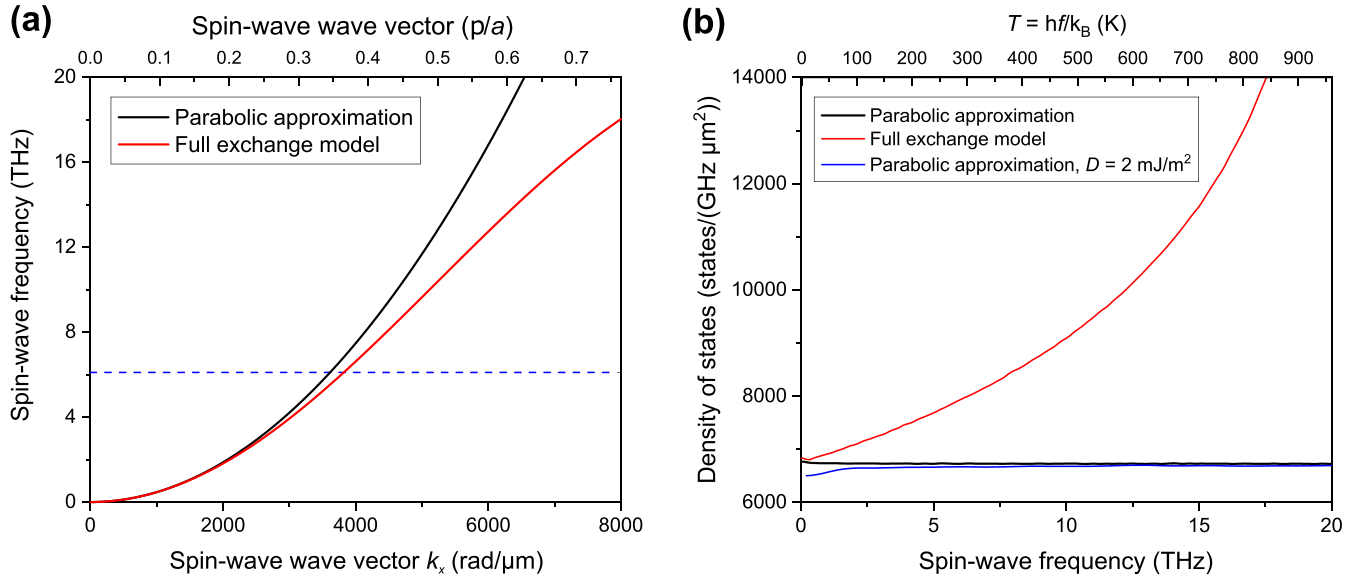

FIG. 1. (a) Spin-wave dispersion for the full Heisenberg model [red, Eq. (A7)] and its parabolic approximation [black, Eq. (A8)] (model details in Appendix, parameters in main text). Dashed-blue line denotes $f = k_B T/h$ for $T = 293$ K, corresponding to the maximum thermal population of spin wave states for this paper. (b) Spin-wave DOS for different dispersion models in 2D: parabolic (black), full-exchange (red), and parabolic with DMI (blue, D = 2 mJ/m^2) models.

D can then be used to extract A [13,16,19]. A key limitation of this technique, especially for stacks lacking multiple repetitions, is that the required labyrinthine domain configuration is achievable only for a narrow range of magnetic layer thicknesses (e.g., 0.1–0.2 nm) [18].

D. Density functional theory

To complement the experimental results, density functional theory (DFT) calculations were performed to estimate A [39,40] on appropriately constructed atomic multilayer slabs. The generalized Bloch's theorem was used to generate spin spirals with wave vectors k directed along the direction of the IP nearest-neighbor atom, and the spiral axis is given by the cross product of the k vector and slab normal with a spiral angle of 90° [40,41]. To extract the symmetric exchange A, the spiral energy density was calculated over a range of wave vectors k and fit to a quadratic function. The accuracy of these methods have been assessed extensively in previous papers, and shown to consistently predict trends similar to experiments [19,42].

III. RESULTS

The values of A extracted from the different techniques introduced in Sec. II are plotted in Fig. 6 and summarized in Table I. Below, we introduce the samples studied in this paper, and discuss the results obtained using the respective measurement techniques.

A. Samples

The multilayer thin film samples studied in this paper were deposited on thermally oxidized Si wafers by DC magnetron sputtering at RT using a Chiron UHV system (base pressure $<5\times10^{-8}$ Torr) from Bestec GmbH. Five sample compositions are examined, with ultrathin ($\leqslant$2 nm) ferromagnetic (FM) layers: Pt/Co(1)/Pt, Ir/Co(1)/Pt, Ir/Fe(0.4)/Co(0.6)/Pt, Pt/Co(2)/Pt, and Ir/Co(2)/Pt. The FM layer thicknesses, in nm, are indicated in parentheses, while all heavy metal layers are 1-nm thick. The stack additionally includes seed layers Ta(4)/Pt(5) for optimal texture, and a Pt(2) cap to protect against oxidation. Of the five samples, only one (Pt/Co(2)/Pt) has a distinct IP easy axis. This sample set is designed to systematically compare the effects of inversion symmetry (symmetric Pt/Co/Pt cf. the rest), FM bilayer [Ir/Fe(0.4)/Co(0.6)/Pt cf. Ir/Co(1)/Pt], and varying FM thickness [Co(1) cf. Co(2)] on A and its experimental determination.

B. BLS spectroscopy and dispersion analysis

BLS measurements were performed using a wave-vector-resolved setup operated in the backscattering geometry [25]. Here, a laser with a wavelength of $\lambda_L = 532$ nm was used and the spectral analysis of the inelastically scattered light was performed using a tandem-Fabry-Pérot interferometer of Sandercock type [43]. The measurements were performed at room temperature, with the external magnetic field applied IP to the magnetic film, with sufficiently large magnitude to saturate each sample in the in-plane direction, while oriented perpendicular to the incident plane of the probing laser light. Wave-vector resolution can be achieved by varying the angle of incidence φ, such that the probed spin-wave wave vector equals $k = 4\pi \sin(\varphi)/\lambda_L$ [25]. For the IP configuration, BLS probes thermally populated magnetostatic surface spin waves described by Eq. (1), which propagate perpendicular to the applied (IP) field. Figure 2(a) shows representative BLS spectra for a chiral multilayer sample. The characteristic asymmetry in the (anti) Stokes spin wave peaks for opposite

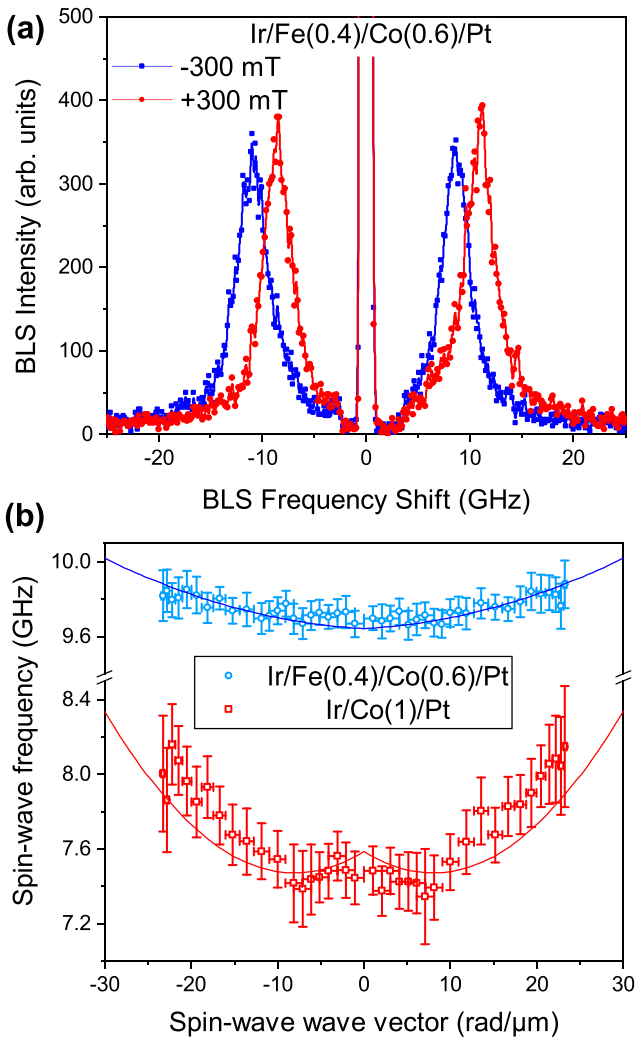

FIG. 2. (a) Representative thermal BLS spectrum for Ir/Fe(0.4)/Fe(0.6)/Pt sample (incidence angle, $\varphi = 45^\circ$) at $\mu_0 H_{\text{ext}} = \pm 300\,\text{mT}$ (red, blue). (b) BLS spectroscopy measurement of the symmetric component of spin-wave dispersion, f_{sym} [from Eq. (1), data markers], and corresponding best fits [Eq. (1)] used to estimate A for two representative samples—Ir/Fe(0.4 nm)/Co(0.6 nm)/Pt (blue, $\mu_0 H_{\text{ext}} = 300\,\text{mT}$) and Ir/Co(1 nm)/Pt (red, $\mu_0 H_{\text{ext}} = 830\,\text{mT}$). Fit parameters are listed in Table I.

field polarities arises from the chiral DMI interaction. For this paper, however, we are mainly interested in the symmetric component of the dispersion. Accordingly, Fig. 2(b) shows representative symmetrized BLS dispersion data obtained for two samples, with the fitted result from the dispersion model [Eq. (1)] overlaid (parameters listed in Table I). This data is obtained by comparing the measurements at opposite directions of the magnetic bias field.

We note from Eq. (1) that the dispersion curvature is also influenced by the anisotropy field H_{U} and the saturation magnetization M_{S}. Hence, the fitted value for A can be influenced by $\mu_0 H_{\text{U}}$, which in turn influences the optimal M_{S} since these two parameters essentially define the ferromagnetic resonance frequency $f(k \to 0)$ (FMR). As a basis for the evaluation of the BLS data, we use the H_{U} and M_{S} values obtained from

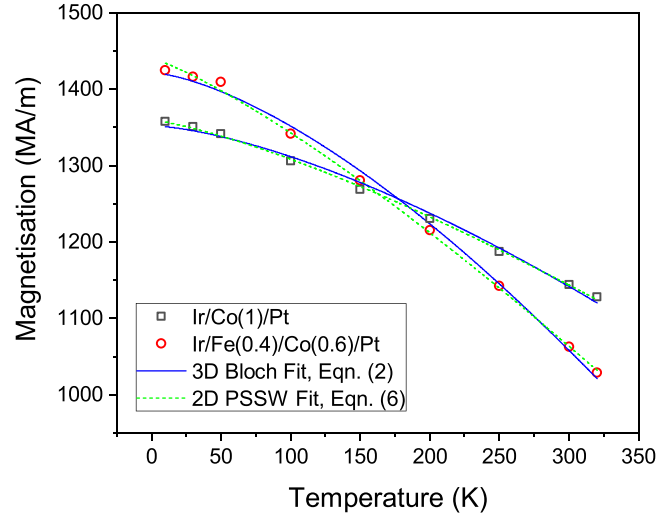

FIG. 3. T dependence of saturation magnetization M_S for samples Ir/Co(1)/Pt (black squares) and Ir/Fe(0.4)/Co(0.6)/Pt (red dots) obtained from the zero-field extrapolation of $M(H)$ hysteresis loops measured by SQUID magnetometry. Lines denote fits to Bloch's $T^{3/2}$ law used to obtain A via the 3D model [solid blue, Eq. (2)] and the 2D PSSW model [dashed green, Eq. (6), third iteration].

SQUID measurements. To estimate the error bar for A caused by the uncertainty of M_{S} and H_{U}, we allow A to vary in either direction until M_{S} needs to altered by ∼15%—corresponding to the uncertainty of M_{S} within VSM measurements. To get a self-consistent modeling, for every M_{S} value, we adjust H_{U} to match the calculated FMR frequency to the frequency measured by BLS for $k \to 0$.

For the Ir/Fe(0.4)/Co(0.6)/Pt sample, the fit thus obtained agrees well with the data for $A = 7\,\text{pJ/m}$, and $\mu_0 H_{\text{U}} = 1433\,\text{mT}$ ($\mu_0 H_{\text{K}} \approx 120\,\text{mT}$). Meanwhile, for the Ir/Co(1 nm)/Pt sample, where the dispersion data shows a much larger slope, the best fit model parameters are $A = 22\,\text{pJ/m}$ and $\mu_0 H_{\text{U}} = 2210\,\text{mT}$ ($\mu_0 H_{\text{K}} \approx 730\,\text{mT}$). In general, we find a good agreement between the H_{K} values obtained from BLS with those from VSM as well as with previous studies on similar material systems [19]. The values of A obtained using Eq. (1) on the BLS data for all other samples are summarized in Fig. 6. We verified that more sophisticated modeling of the dispersion relation (see Appendix) using a layer resolved numerical approach, which allows, e.g., for a distribution of material parameter across the film thickness, gives values for A, which are in agreement with those obtained from Eq. (1) within the error bars. Note that the error bars for A using BLS are comparatively large, as it requires the experimental determination of several parameters, each using different techniques, and with different dependencies. A detailed list of values for the relevant material parameters for all samples is provided in Table I.

C. $M_{\text{S}}(T)$ results and analysis

Figure 3 shows representative $M_{\text{S}}(T)$ data obtained from the same two samples—Ir/Fe(0.4)/Co(0.6)/Pt and Ir/Co(1)/Pt—from $M(H)$ hysteresis loops obtained by SQUID

magnetometry measurements at varying temperatures in the IP configuration. The measured $M_S(T)$ data were fit with Bloch's $T^{3/2}$ law using: (a) the 3D value for η, (b) the thickness corrected η values [23], and (c) the model including PSSW modes [Eq. (6)], as shown in Fig. 3. To fit Eq. (6), ω_0 was first estimated using the midpoint of the used $M(H)$ field range, i.e., $\omega_0 = \gamma\mu_0(H_{ext} + H_U - M_S)$ [44], and was then used in Eq. (6) to estimate A using an iterative fitting procedure (see Appendix for details). Here, M_S was estimated by extrapolating $M_S(T)$ data to $T = 0$, while H_U was extracted from BLS measurements modelled by Eq. (1).

The values of A obtained from the various $M_S(T)$ models are plotted in Fig. 6, and detailed in Table I. We find that the modified η version of Bloch's law ($\eta \approx 0.3(0.17)$ for $t = 1(2)$ nm [23]) returns the highest values for A, providing the best agreement with those obtained from BLS and DFT. Incidentally, the $M_S(T)$ measurements were repeated in the OP configuration, with no observable differences in the resulting A values cf. IP results, in line with the expected negligible influence of DMI on the spin-wave DOS [cf. Fig. 1(b)]. Separately, we also performed direct measurements of the T dependence of magnetization, i.e., $M(T)$ at fixed applied fields above saturation ($H > H_S$). While this latter approach allows for a more precise estimation of ω_0 in Eq. (6), we find excellent agreement of the obtained A values with the hysteresis loop method. A detailed description of these quantitative comparisons is provided in the Appendix.

D. Domain periodicity

Domain periodicity determination of A requires imaging of the magnetic texture configuration at remanence. Of the five samples studied, only Ir/Fe(0.4)/Co(0.6)/Pt can stabilize a ZF domain configuration [Fig. 4(a)]. As a result, domain periodicity analysis could not be performed on the other four samples—for Pt/Co(1)/Pt and Ir/Co(1)/Pt, because of their high remanent magnetization, and for Co(2) samples, due to their IP easy axis—both of which result in the lack of domain nucleation at remanence.

The domain imaging was performed using Lorentz transmission electron microscopy (LTEM) with an FEI Titan S/TEM operated in Fresnel mode at 300 kV. A dedicated Lorentz lens, used to focus the electron beam, was used at a defocus of −1.8 mm, while the objective lens located at the sample position was switched off for field-free image acquisition. In order to obtain sufficient magnetic contrast for LTEM, a two-repeat version of the stack, i.e., $[Ir/Fe(0.4)/Co(0.6)/Pt]_2$, was used. Despite the weak signal in real space, the signature "split-ring" structure of the labyrinthine domain configuration is clearly visible in frequency space, which allows us to obtain a domain period of 87 nm. Micromagnetic simulations were performed using MuMax^3 [45] for an array of D and A values [Figs. 4(b) and 4(c)], with M_S and uniaxial anisotropy (K_u) parameters obtained from magnetometry. Subsequently, the real space magnetization of each simulation was Fourier-transformed to extract the period (P), which was fit to a low-order 2D polynomial: $P = a_0 + a_1 D + a_2 A + a_3 D \cdot A$ ($R^2 = 0.99$). By constraining the fit to the measured period (87 nm) and

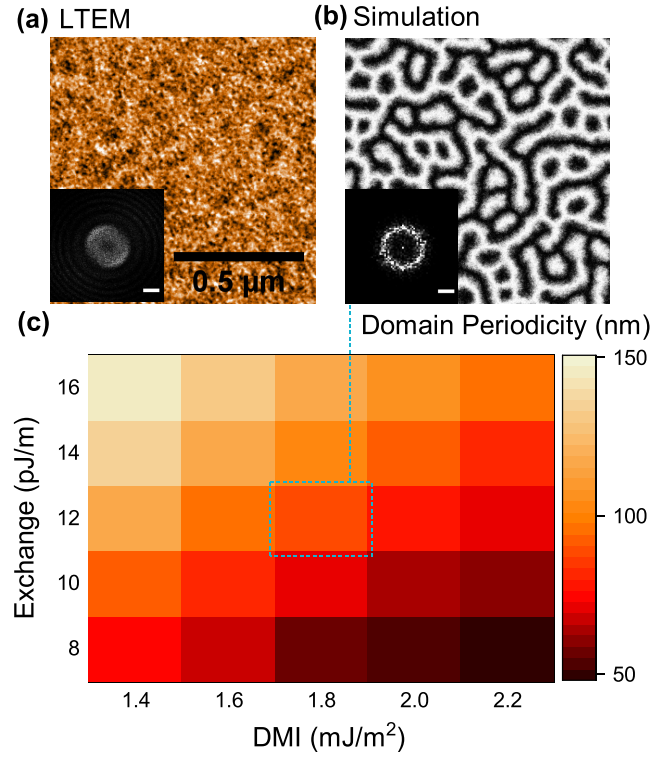

FIG. 4. Zero-field domain periodicity analysis for sample $[Ir/Fe(0.4)/Co(0.6)/Pt]_2$. (a) Lorentz TEM image and (b) micromagnetically simulated magnetization (M_z) with D, A parameters closest to the best fit (scalebar: 0.5 μm). Insets show Fourier transforms (scalebar: 10 μm^{-1}). (c) Simulated domain periodicity for an array of D, A values. Dashed box shows the closest match to experiment [i.e., (b)].

$D = 1.72$ mJ/m^2 (measured by BLS), A was determined to be 11.1 pJ/m.

E. DFT calculations

DFT calculations were implemented on atomic multilayer slabs with compositions $PtCo_{[5]}Pt$, $IrCo_{[5]}Pt$, $IrFe_{[2]}Co_{[3]}Pt$, $PtCo_{[9]}Pt$, and $IrCo_{[9]}Pt$, where subscripts (in brackets) for Fe and Co represent the number of atomic layers. As each Fe (Co) atomic layer is about 0.2 nm thick, these slabs approximately correspond to the five experimentally studied samples. Each slab is separated by a vacuum of 10 Å in the normal direction to prevent spurious inter-cell interactions, the IP lattice constant is set to the bulk Ir value, and exchange-correlation approximated by the Perdew-Burke-Ernzerhof formulation of the generalized gradient approximation [46]. The energy densities for spin spiral configurations were calculated for wave vectors k up to ~6000 rad/μm (0.6 rad/Å), as shown in Fig. 5 (see Sec. II for details). The spiral energy shows approximately quadratic dependence on k, and low wave vectors, and progressively deviates from parabolic behavior at large k. For the $IrFe_{[2]}Co_{[3]}Pt$ case, we additionally note appreciable softening of the spin spiral at $k \sim 800$ rad/μm (0.08 rad/Å). This phenomenon has been observed in IrFe slabs, and attributed to Ir-Fe hybridization [47].

To determine A, we fit the spiral energy densities to a quadratic function in k over varying ranges of k, which yield

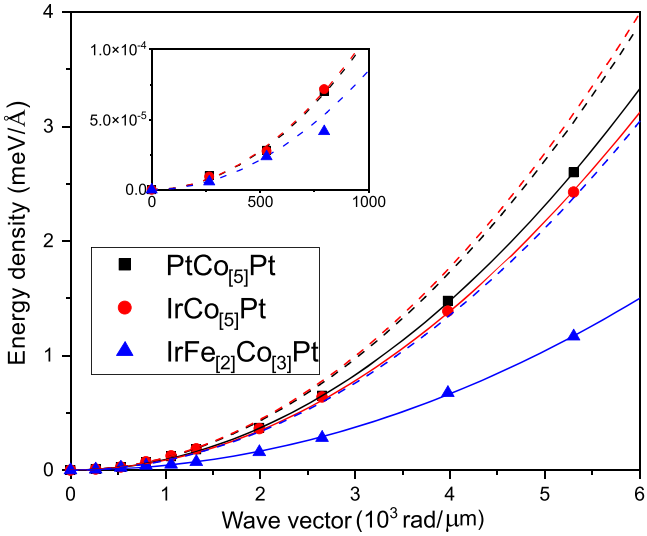

FIG. 5. DFT-computed dispersion of spin spiral energy densities for the three 1-nm samples studied in this paper. Inset shows a zoom-in view of the small-k region (k axis in rad/μm). Dashed (solid) lines are quadratic fits for small (large) k values, respectively.

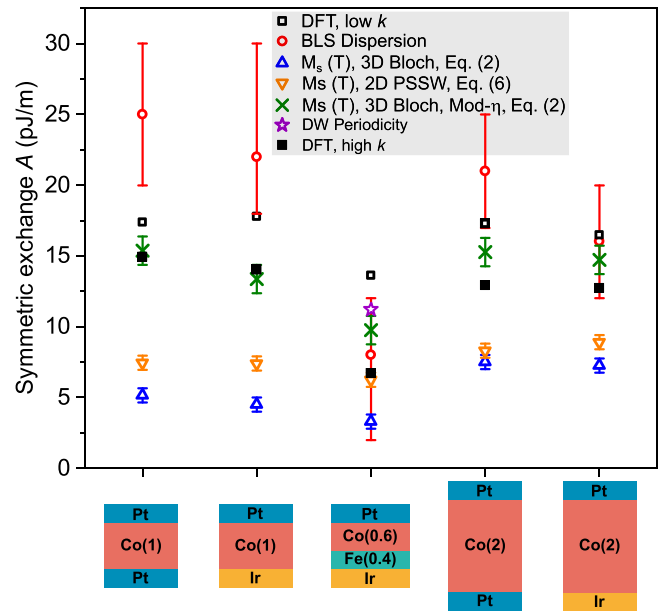

FIG. 6. Exchange stiffness, A of the five studied samples, obtained by different methods detailed—BLS dispersion, $M_S(T)$ modeling (3D Bloch law, modified η, PSSW model), domain periodicity, and DFT calculations (low k, high k). Bottom inset shows stack schematics for the respective samples, dashed black line separates the 1-nm FM and 2-nm FM samples for clarity.

different results due to the deviation from parabolicity. For the small k limit, we fit to energies with $k < 1200$ rad/μm (0.12 rad/Å), while for large k, we fit over all the data shown in Fig. 5. Overall, the DFT-computed results, shown in Fig. 6 and Table I, give the largest exchange for slabs with pure Co layers, and lower with the introduction of Fe. Small variations are observed with varying heavy metal layers (Pt/Co/Pt cf. Ir/Co/Pt) and Co thickness (1 nm Co cf. 2 nm Co). Finally, the A obtained for small k is consistently larger than that obtained over a larger k range—most notably by ∼2× for $IrFe_{[2]}Co_{[3]}Pt$. This difference is reasonable considering that the spin spiral dispersion flattens near the BZ boundaries, and is relevant to the observed discrepancies in A between BLS and $M_S(T)$ measurements (see Sec. IV).

IV. DISCUSSION

The key result of this paper, presented in Fig. 6 and Table I, compares the A values of five multilayer samples obtained using the different methods detailed above. Overall, we find that the A values from different methods do not coincide within errors bars for any sample, with up to 2–5× discrepancies within each sample across techniques. We conclude that these deviations between techniques are likely of systematic nature, and may arise from the specific assumptions and limitations of the methods for ultrathin ferromagnets, discussed further

TABLE I. Measured values of the key magnetic parameters for the five studied samples, and the measurement techniques used. VSM was used to determine M_S (OP), and anisotropy parameters K_U and K_{eff}. The K_U and K_{eff} obtained from BLS deviate from these values by less than 10%. FMR is used to obtain γ (Fig. 9, ∗ Pt/Co(1)/Pt, Ir/Co(1)/Pt assumed to have the same γ as measured for their 2-nm-thick counterparts.). The values of exchange stiffness, A, obtained by BLS dispersion, $M_S(T)$ modeling (3D Bloch law, modified η, PSSW model), LTEM domain periodicity, and DFT calculations (low k, high k) are listed for comparison (methods and parameters detailed in Sec. III).

Parameter	**Technique**	Pt/Co(1)/Pt	Ir/Co(1)/Pt	Ir/Fe(0.4)/Co(0.6)/Pt	Pt/Co(2)/Pt	Ir/Co(2)/Pt
M_S (kA/m)		1430 ± 220	1280 ± 190	1200 ± 180	1330 ± 200	1200 ± 190
K_U (MJ/m^3)	VSM	1.93 ± 0.29	1.54 ± 0.23	0.86 ± 0.13	0.81 ± 0.12	0.89 ± 0.13
K_{eff} (MJ/m^3)		0.63 ± 0.09	0.50 ± 0.08	-0.05 ± 0.05	-0.12 ± 0.05	0.24 ± 0.05
γ (rad/($T \cdot$ ns))	FMR	184.96 ± 0.87*	167.50 ± 0.13*	167.88 ± 0.19	184.96 ± 0.87	167.50 ± 0.13
	BLS	25 ± 5	$22 + 8/-4$	$7 + 8/-4$	21 ± 4	16 ± 4
	$M_S(T)$: $T^{3/2}$, Eq. (2)	5.18 ± 0.50	4.51 ± 0.50	3.3 ± 0.50	7.52 ± 0.50	7.25 ± 0.50
	$M_S(T)$: PSSW, Eq. (6)	7.45 ± 0.51	7.41 ± 0.23	6.26 ± 0.24	8.33 ± 0.32	8.91 ± 0.35
A (pJ/m)	$M_S(T)$: $T^{3/2}_{\mathbf{mod}\,\eta}$, Eq. (2)	15.38 ± 1.00	13.39 ± 1.00	9.78 ± 1.00	15.27 ± 1.00	14.73 ± 1.00
	LTEM, Periodicity			11.1		
	DFT, low k	17.4	17.8	13.6	17.3	16.5
	DFT, high k	14.9	14.0	6.7	12.9	12.7

below. As the first cross-technique comparison of exchange stiffness in ultrathin FMs to our knowledge, our paper may offer a viable explanation of the large spread of A values reported on similar ultrathin films [9,22,24,27,48].

Reassuringly, however, a qualitative comparison of techniques reveals that the evolution of A across samples with the same FM thickness follows a similar trend. For example, for the 1-nm thick FM samples, all methods report A values for Pt/Co(1)/Pt that are comparable or larger than that for Ir/Co(1)/Pt, while that for Ir/Fe(0.4)/Co(0.6)/Pt is considerably lower. The decrease in A upon introducing Fe, also noted by DFT, is consistent with the lower exchange for bulk Fe compared to bulk Co [49]. Additionally, interfacial hybridization effects, which assume increased significance for ultrathin films, may also play a role in the trend observed across the 1-nm and 2-nm FM samples [50–52].

Meanwhile, comparing across techniques for any given sample, we find that BLS analysis consistently reports the largest magnitude for A. Note that the the large error bars for BLS in Fig. 6 reflect the inherent challenges in the determination of A from BLS spin-wave spectra for ultrathin films with strong OP anisotropy, due to the intermixing of the different contributions in Eq. (1). However, even within their error bars, most A values from BLS are considerably larger than the ones obtained from other methods. As an interesting aside, we note that recent comparative measurements of the DMI, D, also reported higher values from BLS measurements than other methods like domain wall expansion [53].

The values obtained from BLS for A are followed by Bloch law (modified η), and the 2D PSSW Bloch law [Eq. (6)]. Finally, the original 3D Bloch $T^{3/2}$ law [Eq. (2)] reports the smallest value of A for the studied ultrathin films. In particular, the A values from the 3D Bloch law are unrealistically low as it does not account for the increased magnon density in ultrathin films [23]. Meanwhile, we expect that the 2D Bloch law, with the iterative use of Eq. (6), should produce closer to those obtained from DFT and other measurement techniques. While this is indeed qualitatively the case, the A values from the 2D Bloch law are still considerably smaller than those from the BLS dispersion. Finally, a similar trend is observed for the Bloch $T^{3/2}$ law with thickness-corrected η, albeit the A values for this case are closer to the BLS values.

The fact that all $M_S(T)$-based methods report considerably lower A values compared to BLS could be attributed to several reasons. One likely source is the assumed parabolic dispersion of the spin wave spectrum, which forms the basis for all techniques used to estimate A—albeit over different ranges of wave vectors. As shown by DFT calculations (Fig. 5), the dispersion softening at higher k results in discrepancies between parabolic fits over different ranges of wave vectors, leading to over $2\times$ variation in the obtained magnitude of A. On one hand, BLS probes the low k limit ($k \lesssim 25$ rad/μm), where the parabolic approximation is expected to hold (Fig. 5: inset). On the other hand, $M_S(T)$-based methods probe a much larger k range of thermal spin wave distribution, which may extend beyond the parabolic dispersion region. Therefore, as seen in Fig. 5, a parabolic fit to the wave vector range probed by $M_S(T)$-based methods would generally lead to an underestimation of A in comparison to, e.g., the full Heisenberg model. Importantly, we caution that for most cases, a simple parabolic approximation may not be justified over the wave vector range probed by the $M_S(T)$-based methods, and the values for A thus obtained should be interpreted with care.

Another aspect to note is that only within the $M_S(T)$ measurements, the higher-order standing spin-wave (PSSW) modes are also indirectly probed. Here, we have modeled the PSSW modes using micromagnetic continuum theory [Eq. (6)], which approaches its limits for the nanometer thick FMs studied here. A recent paper suggests that PSSW modes in ultrathin films may be renormalized to lower energies along the OP direction, while retaining their dispersion for the IP direction [54]. To test this effect, we halve the frequencies of the PSSW modes compared to Eq. (5) for Ir/Co(1)/Pt within the 2D PSSW model [Eq. (6)], in line with the renormalization factor found in [54]. We find that this results in an increase of the modelled exchange stiffness by about 20% compared to Eq. (5), which uses the micromagnetic continuum approach. This suggests that detailed modeling of the PSSW mode characteristics can at least partially account for the observed reduction of A from $M_S(T)$ methods compared to BLS measurements.

The accuracy of $M_S(T)$ modeling may be further improved by also incorporating single particle excitations, as well as higher-order exchange interactions. On one hand, single particle excitations would increase the $M_S(T)$ reduction, leading to an underestimate of A [34]. Therefore, incorporating these would reduce the discrepancy of A cf. BLS results. On the other hand, higher-order exchange interactions may be able to capture the more complex wave vector dependence of the exchange energy density [55,56]. However, incorporating these would drastically increase the resources needed to extend the respective models, and may complicate the extraction of the Heisenberg exchange contribution.

Other sources of discrepancy to be considered are the potential presence of a dead layer within the magnetic film, and proximity-induced magnetization effects within the neighboring heavy metals. Both of these would the effective FM thickness, and therefore directly influence the results from all three $M_S(T)$ models. The FM thickness also governs the dipolar interaction in the spin-wave dispersion relation, leading to an additional uncertainty. However, seeing as the measured M_S for these ultrathin samples is typically around 1200 kA/m at RT, largely in line with reported values for similar stacks [57], we expect the net contribution of dead layer and magnetic proximity effects [58] to be negligible in this case.

In this paper, we have refrained from any T-dependent renormalization of the A values obtained from $M_S(T)$ measurements. In principle, the need for such renormalization arises as the $M_S(T)$ models putatively estimate A for $T = 0$, while the BLS-measured A value is for room temperature. Some previous papers have implemented such renormalization using *ab initio* electronic structure calculations of bulk Co to relate the decrease of $A(T)$ with temperature to that of $M_S(T)$, and to thereby obtain a scaling law for $A(M_S(T))$ [59]. However, our paper has not applied any such T-dependent renormalization to our $M_S(T)$ analysis for several reasons. First, an accurate renormalization treatment would, in principle, require similar *ab initio* calculations for each of our thin film samples, as their electronic structure may differ considerably from the

previously considered bulk Co case [59], which does not account for finite thickness and interface effects. Second, and more importantly, the derivation of Bloch's law and all its 2D variants explicitly assume the constancy of A over the measured temperature range. Therefore, the inclusion of T dependence of A within the measured temperature range is inconsistent with the use of Bloch's law in its current form. Moreover, we further note that the approximation of a T-independent A fits the measured $M_S(T)$ data up to room temperature with very high accuracy. Thus, even if the present form of Bloch's law is revised to incorporate T dependence of A, such a fit may be expected to instead overparametrize the problem, resulting in potentially spurious estimates. Finally, we emphasize that any T-dependent renormalization [59] would lower the A values resulting from $M_S(T)$ measurements. Thus, the lack of such renormalization cannot account for our findings of consistently lower A values from $M_S(T)$ measurements as compared to other methods.

V. CONCLUSIONS

In summary, this paper presents a quantitative comparison of the determination of the Heisenberg exchange stiffness, A, across five multilayer films comprising ultrathin ferromagnets using different methods, viz., BLS dispersion, $M_S(T)$ reduction via three models (conventional 3D Bloch law, 3D Bloch law with modified η, 2D Bloch law with PSSW modes), domain periodicity, and DFT calculations. Despite the exchange interaction being arguably the most fundamental property of magnets, and its crucial role in determining material viability for device applications, we find that a thorough understanding of its magnitude in the ultrathin film limit and its dependence on interfacial and stack properties is lacking.

While qualitative trends are apparent across samples, we note $2-5\times$ discrepancies in the magnitude of A obtained by the various methods, underscoring the complexity of its determination in the ultrathin limit. In general, methods using $M_S(T)$ models report lower A values compared to BLS spin-wave dispersion analysis. Qualitatively, these discrepancies may arise, e.g., from the different wave-vector ranges probed by these methods, and the deviation of the spin-wave dispersion from the assumed parabolicity used to determine A. In other words, it shows here that the exchange constant A is obtained from an approximation of the Heisenberg model that assumes a small variation in the orientation of the local magnetic moments, which is only insufficiently fulfilled in many cases, especially for many $M_S(T)$ measurements. Additionally, accurate modeling of $M_S(T)$ data requires accounting for additional effects that emerge at the ultrathin limit, such as reduced dimensionality and confinement modes [32].

In particular, we find that the analysis and interpretation of $M_S(T)$ data for ultrathin films is far from trivial, as the underlying models contain numerous assumptions that are only partially satisfied [32]. As a general consequence, when using A to describe the exchange interaction in ultrathin films, one must be duly mindful of the implicit approximations, which depend on the relevant length scales or wave vectors. Therefore, when modeling ultrathin films, it may be advantageous to use A values that are obtained by methods considering length scales similar to the problem at hand. In general, it is advisable to quantify the accuracy of a measurement of A using a systematic assessment, i.e., values from methods with small wave vectors (e.g., BLS) should rather be considered as upper limit for A while values from $M_S(T)$ measurements can be considered as lower limit. For an improved determination of A with the help of $M_S(T)$ measurements, a numerical modeling of $M_S(T)$ with the nonapproximated spin-wave dispersion including an accurate treatment of high wave vectors and dimensionality effects could be beneficial, but this approach might easily lead to an overparameterisation of the problem. Additionally, our results would also improve the interpretation of other measured micromagnetic parameters such as DMI, whose extraction from experimental data typically includes the estimation of A.

ACKNOWLEDGMENTS

We acknowledge the support of the National Supercomputing Centre (NSCC), Singapore for computational resources. This work was supported by the SpOT-LITE program (A*STAR Grant No. A18A6b0057) funded by Singapore's RIE2020 initiatives, and by NUS funds (Grant No. A-0004544-00-00). Funding by the Deutsche Forschungsgemeinschaft within the CRC TRR173 *Spin+X* [No. 268565370 (Projects B01 and B11)] and within the Priority Program SPP2137 *Skyrmionics* (Project No. 403512431) is gratefully acknowledged.

APPENDIX

The Appendix consists of four sub-sections: Sec. A1 discusses the details of the temperature-dependent measurement of saturation magnetisation, Secs. A2 and A3 discuss the applied models of spin-wave dispersion relations and their approximations, and Sec. A4 gives the details of the ferromagnetic resonance measurements.

1. $M(T)$ measurements and analysis

The $M_S(T)$ data in Fig. 3 was obtained from $M(H)$ measurements over fields above saturation, $H > H_S$, for several fixed temperatures. To remove substrate contributions, the measured $M(H)$ for $H > H_S$ was fit to a straight line. The negative slope, resulting from the diamagnetic substrate, was removed by extrapolation to $H = 0$. The magnetization was then calculated in intensive units (MA/m) by accounting for sample dimensions. The Fig. 7(a) shows the measured $M(H)$ data over fields above saturation at different fixed temperatures for the Ir/Co(1)/Pt sample in OP configuration.

For comparative purposes, additional magnetometry measurements were performed to quantify $M(T)$ at fixed external fields. A key advantage of this fixed field method is that the spin-wave dispersion relation (i.e., the dipolar gap ω_0) is unchanged during the measurement, which, in principle allows the use of Eqs. (3) and (6) without any approximations. However, in this case, removing the substrate contribution to the measured $M(T)$ requires additionally a reference measurement of the bare substrate, whose dimensions and weight need to be identical to the sample of interest. Figure 7(b) shows the measured $M(T)$ data at different fixed fields for the Ir/Co(1)/Pt sample in OP configuration. To circumvent

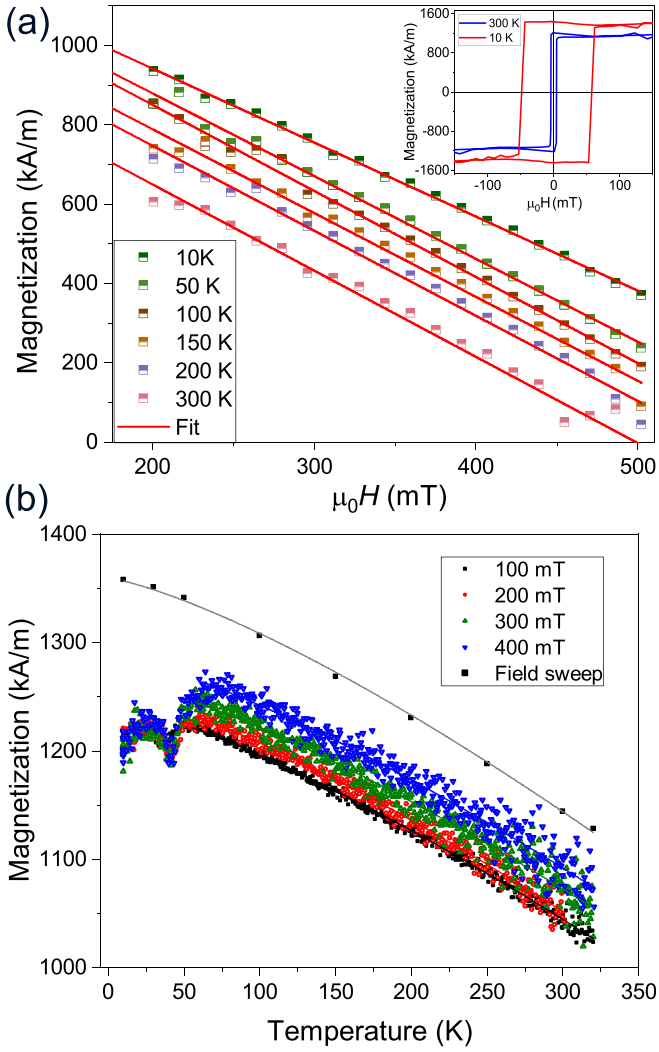

FIG. 7. (a) $M(H)$ measurements for Ir/Co(1)/Pt measured in OP geometry at fixed temperatures over $10-300$ K for fields, $H > H_s$. The data were linearly fitted (red), and their extrapolation to ZF was used to determine M_S for each temperature. Inset shows corresponding $M(H)$ hysteresis loop measurements at 10 K (red) and 300 K (blue). (b) $M(T)$ measurements for Ir/Co(1)/Pt sample obtained in OP geometry at several fixed fields (100–400 mT), and from $M(H)$ extrapolation (black, from Fig. 3). Deviations in $M(T)$ for $T \lesssim 50$ K are due to residual oxygen [60]. Solid lines are fits to the 2D PSSW model, Eq. (6).

the deviations observed for $T \lesssim 50$ K, known to arise from residual oxygen [60], $M(T)$ data for $T < 70$ K have been omitted from the fits [Fig. 7(b), solid lines].

As the thermal occupation of states is highest for the fundamental spin-wave mode, the dipolar gap ω_0 is a crucial parameter for the reliable use of $M_S(T)$ models for ultrathin films [Eqs. (3) and (6)]. First, for $M(H)$ measurements involving the extrapolation method, ω_0 was estimated using the center-point of the covered field range as $\mu_0 H_{ext}$, together with the M_S value obtained from the $M_S(T)$ extrapolation, and the anisotropy field $\mu_0 H_U$ extracted from BLS measurements. Using these, we have [44]

$$\omega_0 = \gamma \mu_0 (H_{ext} + H_U - M_S) \quad , \tag{A1}$$

TABLE II. Magnitude of dipolar gap ω_0 [Eq. (A1)] for the $M(T)$ and $M(H)$ measurements performed on sample Ir/Co(1)/Pt over varying external fields in OP configuration, and the resulting A values obtained from the 3D Bloch law and 2D PSSW $M_S(T)$ models.

$\mu_0 H_{ext}$	$\omega_0/(2\pi)$ (GHz)	$A_{T^{3/2}}$ (pJ/m)	A_{PSSW} (pJ/m)
100 mT	20	4.41 ± 0.50	6.98 ± 0.50
200 mT	23	4.35 ± 0.50	6.79 ± 0.50
300 mT	25	4.56 ± 0.50	7.06 ± 0.50
400 mT	28	4.61 ± 0.50	7.03 ± 0.50
Field sweep	25	4.51 ± 0.50	7.05 ± 0.50

with $\mu_0 H_{ext} = 300$ mT. Meanwhile, for $M(T)$ measurements at fixed fields, ω_0 can be reliably determined given the constancy of $\mu_0 H_{ext}$.

To estimate A using the $M_S(T)$ PSSW model, we perform the following iterative procedure to account for the implicit A dependence of the PSSW modes ω_1 and ω_2. We start with the above mentioned estimation of the fundamental frequency ω_0, and use it to evaluate the strict 2D model [Eq. (3)]. This gives a lower estimate of A, which we then use, together with the $M_S(T = 0)$ estimate and the film thickness, t, to calculate ω_1 and ω_2. These frequencies are used to fit the more precise 2D PSSW model [Eq. (6)] up to $n = 2$ to the data. We iterate this fit twice using recalculated PSSW frequencies. The resulting A varied by $<1\%$ between the second and third iterations.

The calculated values of ω_0 are listed in Table II for the different $\mu_0 H_{ext}$ values used in $M(T)$ and $M(H)$ measurements, together with the resulting A values obtained from fits to the Bloch's $T^{3/2}$ law, and the 2D PSSW model [Eq. (6)]. The A values are in good agreement across different $\mu_0 H_{ext}$ values, confirming that both $M(H)$ and $M(T)$ magnetometry data can be used to determine A equally well, with appropriate estimation of ω_0.

2. Numerical modeling approach: Effective exchange stiffness for FM bilayers

One of the five samples used in this paper is a bilayer FM, Fe/Co. To model spin-wave dispersions of thin films with inhomogeneous material parameters across their thickness, numerical calculations [61] and numerical modeling [62] may serve as valuable tools. First, we note that for the other four single magnetic layer films, modeling using Ref. [62] gives A values consistent with Eq. (1), within errors bars. For example, using the Ref. [62] approach to localize the uniaxial anisotropy only on one surface, gives similar results to the effective volume anisotropy approach [Eq. (1)], as the exchange interaction enforces homogeneous dynamics across the ultralow film thickness.

To model the effective dispersion of the Fe/Co bilayer and determine its effective exchange parameter A, we compare results from Eq. (1) to an advanced dispersion model, with arbitrary distribution of M_S, H_U, and A over the film thickness [62]. We thereby verify that the spin-wave dispersion in ultrathin FM bilayers can be well described using an effective A. To do so, first, we numerically calculated the dispersion of the fundamental mode for bilayer $Fe(t_{Fe})/Co(t - t_{Fe})$ with $t = 1$ nm, over IP wave vectors -3000 rad/μm to $+3000$ rad/μm,

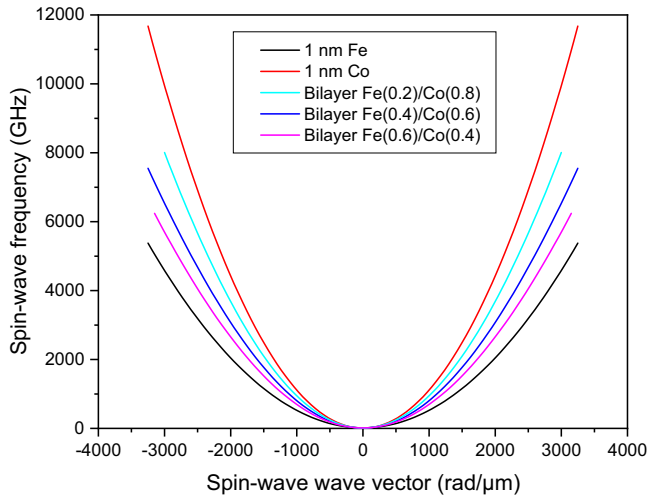

FIG. 8. Spin-wave dispersion of pure Co, pure Fe, and Fe/Co bilayer films, obtained by numerical modeling (parameters in text). Parabolic fits to the data are used to assess the validity of several analytical models to estimate A for bilayers.

using expected values for Co: $M_S^{(Co)} = 1050\,\mathrm{kA/m}$, $A_{Co} = 20\,\mathrm{pJ/m}$, and for Fe, $M_S^{(Fe)} = 1600\,\mathrm{kA/m}$, and $A_{Fe} = 14\,\mathrm{pJ/m}$ as shown in Fig. 8. We fit the data to a function of the form

$$f_{SW}(k) = \frac{\gamma}{2\pi}\frac{2A}{M}\cdot k^2 = \beta_{num}k^2. \tag{A2}$$

Here, β_{num} is a proportionality factor given by $\beta_{num} = (\gamma\mu_0/2\pi)\cdot\lambda_{ex,eff}$, where $\lambda_{ex,eff}$ is the effective spin-wave stiffness. In order to compare different analytical approaches to the numerical data, we evaluate the following model relations between the individual and bilayer exchange stiffnesses:

$$\beta_1 = \beta_{Fe}\cdot\frac{t_{Fe}}{t} + \beta_{Co}\cdot\frac{t_{Co}}{t} \tag{A3}$$

$$\beta_2 = \frac{\gamma}{\pi}\frac{(A_{Fe}+A_{Co})/2}{\left(M_S^{(Fe)}\cdot t_{Fe} + M_S^{(Co)}\cdot t_{Co}\right)/t} \tag{A4}$$

$$\beta_3 = \frac{\gamma}{\pi}\frac{A_{Fe}\cdot t_{Fe} + A_{Co}\cdot t_{Co}}{M_S^{(Fe)}\cdot t_{Fe} + M_S^{(Co)}\cdot t_{Co}}. \tag{A5}$$

Here, β_{Fe} and β_{Co} are the curvatures fitted to the numerically evaluated dispersion data for 1-nm thick Fe and Co films, respectively.

TABLE III. Effective exchange stiffness values for 1-nm Fe/Co bilayers with varying compositions ($t_{Co} = 1 - t_{Fe}$), obtained by fitting the spin-wave dispersion using analytical models $\beta_{1,2,3}$ [Eqs. (A3)–(A5)]. Comparison to the numerical model, β_{num}, yields best agreement for β_3 [Eq. (A5)].

t_{Fe} (nm)	β_{num}	β_1	β_2	β_3
		$[10^{-4}\,\mathrm{GHz/(rad/\mu m)}]$		
0.2	9.03	9.85	8.21	9.08
0.4	7.36	8.66	7.50	7.76
0.6	6.42	7.47	6.90	6.66

Table III lists the values obtained for the different effective exchange models. It is apparent that the β_3 model [Eq. (A5)] best describes the numerically obtained exchange stiffness for bilayer films. This result also underlines that within the micromagnetic framework, the parabolic dispersion approximation for $M(T)$ analysis can be extended to bilayer samples, while appropriately accounting for the thickness weighting of A and M_S, as described by β_3 [Eq. (A5)]. We have also verified that the strength of exchange coupling between the two layers plays at best a minor role. As long as the layers were FM coupled, we observed no effect of the interlayer coupling strength on the effective dispersion, in line with our T-dependent texture evolution studies on similar samples [63].

3. Full and parabolic spin-wave dispersion models

Since each thermally excited magnon reduces $M_S(T)$ by $g\mu_B$, the resulting $M_S(T)$ is given as

$$M_S(T) = M_S(0) - g\mu_B\sum_{\vec{k}} n(\vec{k},T)$$

$$= M_S(0) - g\mu_B\int_0^\infty N(\omega,T)D(\omega)d\omega. \tag{A6}$$

where $n(\vec{k},T)$ is the magnon density per unit volume, which, can be expressed as the product of the DOS $D(\omega)$ and the Bose-Einstein distribution factor $N(\omega)$ [Eq. (4)]. This is the basis of the model leading to Eqs. (2) and (6). Meanwhile, the full spin-wave dispersion for the Heisenberg model on a 2D square lattice can be described as [64]

$$\omega(k)_{full} = \omega_0 + \frac{2\gamma\mu_0\lambda_{ex}}{a^2}(2 - \cos(k_x a) - \cos(k_y a)), \tag{A7}$$

where a is the atomic lattice constant, and the 2D lattice is oriented in the xy plane with spin-wave wave-vector components k_x and k_y. The ensuing parabolic approximation to the dispersion relation is then given by

$$\omega(k)_{parabolic} = \omega_0 + \frac{\gamma\mu_0\lambda_{ex}}{a^2}\left(k_x^2 + k_y^2\right)a^2. \tag{A8}$$

The dispersions of the full model and the parabolic approximation are compared in Fig. 1(a), for a representative set of parameters (see main text). The increasing deviation between the models at larger frequencies hints at the complexity in accurately describing the measured $M_S(T)$ dependence at room temperature. This can be further understood by evaluating the corresponding DOS $\rho(\omega)$, performed here numerically. The DOS is given by the number of available states per frequency interval $d\omega$ around ω such that

$$\rho(\omega) = \frac{1}{S}\sum_{\vec{k}\in K}\delta(\omega - \omega(\vec{k})), \tag{A9}$$

where S and K are the total surface area in real and k space, respectively. It is evident that the full Heisenberg model [Eq. (A7)] gives a larger DOS compared to the parabolic approximation [Eq. (A8)].

To calculate the DOS in the presence of DMI, a k-linear term is added to the dispersion relation [23,29,65]

$$\omega_{DMI}(k) = \frac{2\gamma}{M_S}Dk_x. \tag{A10}$$

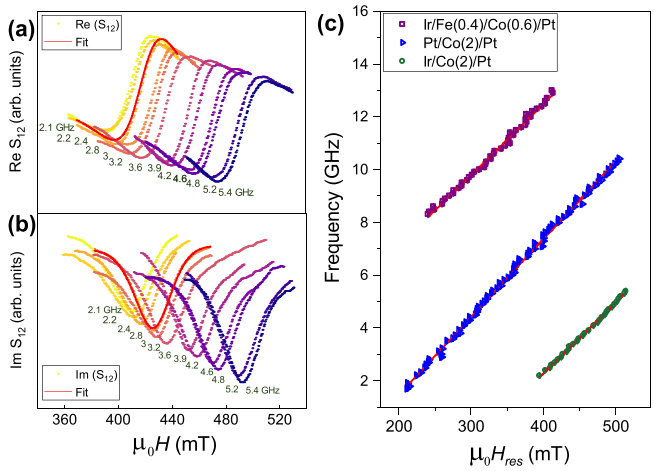

FIG. 9. [(a) & (b)] Exemplary real and imaginary parts of complex transmission parameter S_{12} for sample Ir/Co(2)/Pt, measured by VNA-FMR in OP sample geometry at fields above saturation, $H > H_S$. (c) Dispersion of resonance field, H_{res} with frequency, determined from Lorentzian fits to resonance spectra [e.g., (a) and (b)] for samples Ir/Fe(0.4)/Co(0.6)/Pt (purple), Pt/Co(2)/Pt (blue) and Ir/Co(2)/Pt (green). Overlaid lines are linear fits to the Kittel formula [Eq. (A11)].

Evidently, the DMI-induced dispersion modification does not significantly influence the DOS [Fig. 1(b), blue curve]. Thus, the $M_S(T)$ dependence is predicted to be very similar for magnetometry measurements in IP (interfacial DMI contribution is expected) and OP (interfacial DMI influence can be neglected) field orientations, which is in very good agreement with our experimental findings.

4. Ferromagnetic resonance measurements

Ferromagnetic resonance (FMR) measurements were performed to determine the gyromagnetic ratio γ using a home-built broadband vector network analyzer (VNA) magnetic absorption spectroscopy setup. The samples were mounted on a coplanar waveguide (CPW) in OP field geometry, and the complex microwave transmission parameter S_{12} was recorded at fixed microwave frequencies, f over 1–14 GHz, as a function of the OP magnetic field ($\mu_0 H_{ext}$, up to ~ 0.55 T). The resulting real and imaginary parts of S_{12}, exemplified in Figs. 9(a) and 9(b) for sample Ir/Co(2)/Pt, were fit to the Lorentzian lineshape functions to determine the resonance field, $\mu_0 H_{res}$, for each frequency.

The resulting H_{res}-f dispersion plot, shown in Fig. 9(c) for the three measured samples, can be fit by the Kittel formula [44] for OP geometry,

$$f = \frac{\mu_0 \gamma}{2\pi}(H_{res} - M_{eff}). \tag{A11}$$

Here, $M_{eff} = M_S - H_U$, the effective magnetization, includes contributions from the uniaxial anisotropy field H_U. The three $H_{res} - f$ plots in Fig. 9(c) show a large variation in their y intercepts, which reflects the anisotropy evolution across samples. Meanwhile, their slopes, proportional to the quantity of interest, γ exhibit marginal ($\sim \pm 5\%$) variation across samples. The observed magnitude of variation of γ across samples, expected to arise from variations in the g factor, is consistent with previous reports on multilayer films [66]. The measured γ values are summarized in Table I, and used in determining A for both BLS and $M(T)$-based methods.

[1] F. Hellman, A. Hoffmann, Y. Tserkovnyak, G. S. D. Beach, E. E. Fullerton, C. Leighton, A. H. MacDonald, D. C. Ralph, D. A. Arena, H. A. Dürr, P. Fischer, J. Grollier, J. P. Heremans, T. Jungwirth, A. V. Kimel, B. Koopmans, I. N. Krivorotov, S. J. May, A. K. Petford-Long, J. M. Rondinelli *et al.*, Interface-induced phenomena in magnetism, Rev. Mod. Phys. **89**, 025006 (2017).

[2] A. Manchon, H. C. Koo, J. Nitta, S. M. Frolov, and R. A. Duine, New perspectives for Rashba spin-orbit coupling, Nat. Mater. **14**, 871 (2015).

[3] A. Soumyanarayanan, N. Reyren, A. Fert, and C. Panagopoulos, Emergent phenomena induced by spin-orbit coupling at surfaces and interfaces, Nature (London) **539**, 509 (2016).

[4] S. S. P. Parkin, M. Hayashi, and L. Thomas, Magnetic domain-wall racetrack memory, Science **320**, 190 (2008).

[5] A. Fert, N. Reyren, and V. Cros, Magnetic skyrmions: advances in physics and potential applications, Nat. Rev. Mater. **2**, 17031 (2017).

[6] A. Hirohata, K. Yamada, Y. Nakatani, I.-L. Prejbeanu, B. Diény, P. Pirro, and B. Hillebrands, Review on spintronics: Principles and device applications, J. Magn. Magn. Mater. **509**, 166711 (2020).

[7] B. Dieny, I. L. Prejbeanu, K. Garello, P. Gambardella, P. Freitas, R. Lehndorff, W. Raberg, U. Ebels, S. O. Demokritov, J. Akerman *et al.*, Opportunities and challenges for spintronics in the microelectronics industry, Nat. Electron. **3**, 446 (2020).

[8] *Ultrathin Magnetic Structures I: An Introduction to the Electronic, Magnetic and Structural Properties*, edited by J. A. C. Bland (Springer-Verlag, Berlin, 2005).

[9] C. A. F. Vaz, J. A. C. Bland, and G. Lauhoff, Magnetism in ultrathin film structures, Rep. Prog. Phys. **71**, 056501 (2008).

[10] M. T. Johnson, P. J. H. Bloemen, F. J. A. d. Broeder, and J. J. d. Vries, Magnetic anisotropy in metallic multilayers, Rep. Prog. Phys. **59**, 1409 (1996).

[11] I. Dzyaloshinsky, A thermodynamic theory of "weak" ferromagnetism of antiferromagnetics, J. Phys. Chem. Solids **4**, 241 (1958).

[12] T. Moriya, Anisotropic superexchange interaction and weak ferromagnetism, Phys. Rev. **120**, 91 (1960).

[13] M. Kuepferling, A. Casiraghi, G. Soares, G. Durin, F. Garcia-Sanchez, L. Chen, C. H. Back, C. H. Marrows, S. Tacchi, and G. Carlotti, Measuring interfacial Dzyaloshinskii-Moriya interaction in ultra thin films, arXiv:2009.11830.

[14] N. Nagaosa and Y. Tokura, Topological properties and dynamics of magnetic skyrmions, Nat. Nanotechnol. **8**, 899 (2013).

[15] W. Jiang, P. Upadhyaya, W. Zhang, G. Yu, M. B. Jungfleisch, F. Y. Fradin, J. E. Pearson, Y. Tserkovnyak, K. L. Wang,

O. Heinonen, S. G. E. te Velthuis, and A. Hoffmann, Blowing magnetic skyrmion bubbles, Science **349**, 283 (2015).

[16] C. Moreau-Luchaire, C. Mouta S, N. Reyren, J. Sampaio, C. A. F. Vaz, N. van Horne, K. Bouzehouane, K. Garcia, C. Deranlot, P. Warnicke *et al.*, Additive interfacial chiral interaction in multilayers for stabilization of small individual skyrmions at room temperature, Nat. Nanotechnol. **11**, 444 (2016).

[17] S. Woo, K. Litzius, B. Krüger, M.-Y. Im, L. Caretta, K. Richter, M. Mann, A. Krone, R. M. Reeve, M. Weigand *et al.*, Observation of room-temperature magnetic skyrmions and their current-driven dynamics in ultrathin metallic ferromagnets, Nat. Mater. **15**, 501 (2016).

[18] O. Boulle, J. Vogel, H. Yang, S. Pizzini, D. de Souza Chaves, A. Locatelli, T. O. Menteş, A. Sala, L. D. Buda-Prejbeanu, O. Klein *et al.*, Room-temperature chiral magnetic skyrmions in ultrathin magnetic nanostructures, Nat. Nanotechnol. **11**, 449 (2016).

[19] A. Soumyanarayanan, M. Raju, A. L. Gonzalez Oyarce, A. K. C. Tan, M.-Y. Im, A. P. Petrović, P. Ho, K. H. Khoo, M. Tran, C. K. Gan *et al.*, Tunable room-temperature magnetic skyrmions in Ir/Fe/Co/Pt multilayers, Nat. Mater. **16**, 898 (2017).

[20] F. Schreiber and Z. Frait, Spin-wave resonance in high-conductivity films: The Fe-Co alloy system, Phys. Rev. B **54**, 6473 (1996).

[21] S. Klingler, A. Chumak, T. Mewes, B. Khodadadi, C. Mewes, C. Dubs, O. Surzhenko, B. Hillebrands, and A. Conca, Measurements of the exchange stiffness of YIG films using broadband ferromagnetic resonance techniques, J. Phys. D **48**, 015001 (2015).

[22] K. Shahbazi, J.-V. Kim, H. T. Nembach, J. M. Shaw, A. Bischof, M. D. Rossell, V. Jeudy, T. A. Moore, and C. H. Marrows, Domain-wall motion and interfacial Dzyaloshinskii-Moriya interactions in Pt/Co/Ir(t_{Ir})/Ta multilayers, Phys. Rev. B **99**, 094409 (2019).

[23] H. T. Nembach, J. M. Shaw, M. Weiler, E. Jué, and T. J. Silva, Linear relation between Heisenberg exchange and interfacial Dzyaloshinskii–Moriya interaction in metal films, Nat. Phys. **11**, 825 (2015).

[24] I. A. Yastremsky, O. M. Volkov, M. Kopte, T. Kosub, S. Stienen, K. Lenz, J. Lindner, J. Fassbender, B. A. Ivanov, and D. Makarov, Thermodynamics and Exchange Stiffness of Asymmetrically Sandwiched Ultrathin Ferromagnetic Films with Perpendicular Anisotropy, Phys. Rev. Appl. **12**, 064038 (2019).

[25] T. Sebastian, K. Schultheiss, B. Obry, B. Hillebrands, and H. Schultheiss, Micro-focused Brillouin light scattering: Imaging spin waves at the nanoscale, Front. Phys. **3**, 1589 (2015).

[26] K. Di, V. L. Zhang, H. S. Lim, S. C. Ng, M. H. Kuok, X. Qiu, and H. Yang, Asymmetric spin-wave dispersion due to Dzyaloshinskii-Moriya interaction in an ultrathin Pt/CoFeB film, Appl. Phys. Lett. **106**, 052403 (2015).

[27] P. J. Metaxas, J. P. Jamet, A. Mougin, M. Cormier, J. Ferré, V. Baltz, B. Rodmacq, B. Dieny, and R. L. Stamps, Creep and Flow Regimes of Magnetic Domain-Wall Motion in Ultrathin Pt/Co/Pt Films with Perpendicular Anisotropy, Phys. Rev. Lett. **99**, 217208 (2007).

[28] P. Pirro, V. I. Vasyuchka, A. A. Serga, and B. Hillebrands, Advances in coherent magnonics, Nat. Rev. Mater. **6**, 1114 (2021).

[29] M. Belmeguenai, J.-P. Adam, Y. Roussigné, S. Eimer, T. Devolder, J.-V. Kim, S. M. Cherif, A. A. Stashkevich, and A. Thiaville, Interfacial Dzyaloshinskii-Moriya interaction in perpendicularly magnetized Pt/Co/AlO_x ultrathin films measured by Brillouin light spectroscopy, Phys. Rev. B **91**, 180405(R) (2015).

[30] B. A. Kalinikos and A. N. Slavin, Theory of dipole-exchange spin wave spectrum for ferromagnetic films with mixed exchange boundary conditions, J. Phys. C: Solid State Phys. **19**, 7013 (1986).

[31] T. Böttcher, K. Lee, F. Heussner, S. Jaiswal, G. Jakob, M. Kläui, B. Hillebrands, T. Bracher, and P. Pirro, Heisenberg Exchange and Dzyaloshinskii–Moriya Interaction in Ultrathin Pt(W)/CoFeB Single and Multilayers, IEEE Trans. Magn. **57**, 1600207 (2021).

[32] R. P. Erickson and D. L. Mills, Thermodynamics of thin ferromagnetic films in the presence of anisotropy and dipolar coupling, Phys. Rev. B **44**, 11825 (1991).

[33] F. Bloch, Zur Theorie des Ferromagnetismus, Z. Phys. **61**, 206 (1930).

[34] T. Maeda, H. Yamauchi, and H. Watanabe, Spin Wave Resonance and Exchange Parameters in fcc Fe-Ni Alloys, J. Phys. Soc. Jpn. **35**, 1635 (1973).

[35] M. H. Seavey and P. E. Tannenwald, Direct Observation of Spin-Wave Resonance, Phys. Rev. Lett. **1**, 168 (1958).

[36] W. Kipferl, M. Dumm, P. Kotissek, F. Steinbauer, and G. Bayreuther, Bloch's law for epitaxial ultrathin dot arrays with uniaxial magnetic anisotropy, J. Appl. Phys. **95**, 7417 (2004).

[37] S. Cojocaru, A. Naddeo, and R. Citro, Modification of the Bloch law in ferromagnetic nanostructures, Europhy. Lett. **106**, 17001 (2014).

[38] N. D. Mermin and H. Wagner, Absence of Ferromagnetism or Antiferromagnetism in One- or Two-Dimensional Isotropic Heisenberg Models, Phys. Rev. Lett. **17**, 1133 (1966).

[39] P. Blaha, K. Schwarz, F. Tran, R. Laskowski, G. K. H. Madsen, and L. D. Marks, WIEN2k: An APW+lo program for calculating the properties of solids, J. Chem. Phys. **152**, 074101 (2020).

[40] R. Laskowski, G. K. H. Madsen, P. Blaha, and K. Schwarz, Magnetic structure and electric-field gradients of uranium dioxide: An *ab initio* study, Phys. Rev. B **69**, 140408(R) (2004).

[41] L. M. Sandratskii, Noncollinear magnetism in itinerant-electron systems: Theory and applications, Adv. Phys. **47**, 91 (1998).

[42] X. Chen, M. Lin, J. F. Kong, H. R. Tan, A. K. Tan, S. Je, H. K. Tan, K. H. Khoo, M. Im, and A. Soumyanarayanan, Unveiling the emergent traits of chiral spin textures in magnetic multilayers, Adv. Sci. **9**, 2103978 (2022).

[43] B. Hillebrands, Progress in multipass tandem Fabry–Perot interferometry: I. A fully automated, easy to use, self-aligning spectrometer with increased stability and flexibility, Rev. Sci. Instrum. **70**, 1589 (1999).

[44] C. Kittel, On the theory of ferromagnetic resonance absorption, Phys. Rev. **73**, 155 (1948).

[45] A. Vansteenkiste, J. Leliaert, M. Dvornik, M. Helsen, F. Garcia-Sanchez, and B. van Waeyenberge, The design and verification of MuMax3, AIP Adv. **4**, 107133 (2014).

[46] J. P. Perdew, K. Burke, and M. Ernzerhof, Generalized Gradient Approximation Made Simple, Phys. Rev. Lett. **77**, 3865 (1996).

[47] K. von Bergmann, S. Heinze, M. Bode, E. Y. Vedmedenko, G. Bihlmayer, S. Blügel, and R. Wiesendanger, Observation of a Complex Nanoscale Magnetic Structure in a Hexagonal Fe Monolayer, Phys. Rev. Lett. **96**, 167203 (2006).

[48] P. M. Shepley, H. Tunnicliffe, K. Shahbazi, G. Burnell, and T. A. Moore, Magnetic properties, domain-wall creep motion, and the Dzyaloshinskii-Moriya interaction in Pt/Co/Ir thin films, Phys. Rev. B **97**, 134417 (2018).

[49] M. Pajda, J. Kudrnovský, I. Turek, V. Drchal, and P. Bruno, *Ab initio* calculations of exchange interactions, spin-wave stiffness constants, and Curie temperatures of Fe, Co, and Ni, Phys. Rev. B **64**, 174402 (2001).

[50] S. Kim, K. Ueda, G. Go, P.-H. Jang, K.-J. Lee, A. Belabbes, A. Manchon, M. Suzuki, Y. Kotani, T. Nakamura *et al.*, Correlation of the Dzyaloshinskii-Moriya interaction with Heisenberg exchange and orbital asphericity, Nat. Commun. **9**, 1648 (2018).

[51] M. Perini, S. Meyer, B. Dupé, S. von Malottki, A. Kubetzka, K. von Bergmann, R. Wiesendanger, and S. Heinze, Domain walls and Dzyaloshinskii-Moriya interaction in epitaxial Co/Ir(111) and Pt/Co/Ir(111), Phys. Rev. B **97**, 184425 (2018).

[52] K. Zakeri, T. Chuang, A. Ernst, L. M. Sandratskii, P. Buczek, H. J. Qin, Y. Zhang, and J. Kirschner, Direct probing of the exchange interaction at buried interfaces, Nat. Nanotechnol. **8**, 853 (2013).

[53] A. Magni, G. Carlotti, A. Casiraghi, E. Darwin, G. Durin, L. H. Diez, B. J. Hickey, A. Huxtable, C. Y. Hwang, G. Jakob *et al.*, Key points in the determination of the interfacial Dzyaloshinskii-Moriya interaction from asymmetric bubble domain expansion, IEEE Trans. Magn. **58**, 1 (2022).

[54] J. Pelliciari, S. Lee, K. Gilmore, J. Li, Y. Gu, A. Barbour, I. Jarrige, C. H. Ahn, F. J. Walker, and V. Bisogni, Tuning spin excitations in magnetic films by confinement, Nat. Mater. **20**, 188 (2021).

[55] S. Banerjee, J. Rowland, O. Erten, and M. Randeria, Enhanced Stability of Skyrmions in Two-Dimensional Chiral Magnets with Rashba Spin-Orbit Coupling, Phys. Rev. X **4**, 031045 (2014).

[56] M. Gutzeit, S. Haldar, S. Meyer, and S. Heinze, Trends of higher-order exchange interactions in transition metal trilayers, Phys. Rev. B **104**, 024420 (2021).

[57] H. K. Tan, R. J. J. Lim, H. L. Seng, J. Shanmugam, H. Y. Y. Ko, X. M. Cheng, V. Putra, Z. X. Xing, A. Soumyanarayanan, and P. Ho, Intermixing induced anisotropy variations in CoB-based chiral multilayer films, J. Phys. D **54**, 354003 (2021).

[58] K. Masgrau, Growth and characterization of magnetic tri-layer of Pt/Co/Ir for novel spintronics applications, Masters thesis, Grenoble University, 2015.

[59] R. Moreno, R. F. L. Evans, S. Khmelevskyi, M. C. Muñoz, R. W. Chantrell, and O. Chubykalo-Fesenko, Temperature-dependent exchange stiffness and domain wall width in Co, Phys. Rev. B **94**, 104433 (2016).

[60] S. Gregory, Magnetic Susceptibility of Oxygen Adsorbed on Graphite, Phys. Rev. Lett. **40**, 723 (1978).

[61] B. Hillebrands, Spin-wave calculations for multilayered structures, Phys. Rev. B **41**, 530 (1990).

[62] M. P. Kostylev, Interface boundary conditions for dynamic magnetization and spin wave dynamics in a ferromagnetic layer with the interface Dzyaloshinskii-Moriya interaction, J. Appl. Phys. **115**, 233902 (2014).

[63] X. Chen, E. Chue, J. F. Kong, H. R. Tan, H. K. Tan, and A. Soumyanarayanan, Thermal Evolution of Skyrmion Formation Mechanism in Chiral Multilayer Films, Phys. Rev. Appl. **17**, 044039 (2022).

[64] J. J. Bible and R. E. Camley, Focusing of high-wave-vector magnons, Phys. Rev. B **95**, 224412 (2017).

[65] K. Di, V. L. Zhang, H. S. Lim, S. C. Ng, M. H. Kuok, J. Yu, J. Yoon, X. Qiu, and H. Yang, Direct Observation of the Dzyaloshinskii-Moriya Interaction in a Pt/Co/Ni Film, Phys. Rev. Lett. **114**, 047201 (2015).

[66] J.-M. L. Beaujour, W. Chen, K. Krycka, C.-C. Kao, J. Z. Sun, and A. D. Kent, Ferromagnetic resonance study of sputtered Co|Ni multilayers, Eur. Phys. J. B **59**, 475 (2007).